Journal of Physics:
Condensed Matter

PURPOSE-LED
PUBLISHING™

ACCEPTED MANUSCRIPT • OPEN ACCESS

Large magnetoresistance and quantum oscillations observed in superconducting β-IrSn 4

To cite this article before publication: Smita R Speer *et al* 2026 *J. Phys.: Condens. Matter* in press https://doi.org/10.1088/1361-648X/ae3c4a

Manuscript version: Accepted Manuscript

Accepted Manuscript is "the version of the article accepted for publication including all changes made as a result of the peer review process, and which may also include the addition to the article by IOP Publishing of a header, an article ID, a cover sheet and/or an 'Accepted Manuscript' watermark, but excluding any other editing, typesetting or other changes made by IOP Publishing and/or its licensors"

This Accepted Manuscript is **© 2026 The Author(s). Published by IOP Publishing Ltd**.

As the Version of Record of this article is going to be / has been published on a gold open access basis under a CC BY 4.0 licence, this Accepted Manuscript is available for reuse under a CC BY 4.0 licence immediately.

Everyone is permitted to use all or part of the original content in this article, provided that they adhere to all the terms of the licence https://creativecommons.org/licences/by/4.0

Although reasonable endeavours have been taken to obtain all necessary permissions from third parties to include their copyrighted content within this article, their full citation and copyright line may not be present in this Accepted Manuscript version. Before using any content from this article, please refer to the Version of Record on IOPscience once published for full citation and copyright details, as permissions may be required. All third party content is fully copyright protected and is not published on a gold open access basis under a CC BY licence, unless that is specifically stated in the figure caption in the Version of Record.

View the article online for updates and enhancements.

This content was downloaded from IP address 146.201.200.251 on 02/02/2026 at 15:25

Large Magnetoresistance and Quantum Oscillations Observed in Superconducting β-$IrSn_4$

Smita Speer[1], Yuriy V. Pershin[2], Joanna Blawat[1,2], John Singleton[3], Rongying Jin[2,1*]

[1]Department of Physics & Astronomy, Louisiana State University, Baton Rouge, LA 70803, USA
[2]SmartState Center for Experimental Nanoscale Physics, Department of Physics and Astronomy, University of South Carolina, Columbia, SC 29208, USA
[3]National High Magnetic Field Laboratory, Los Alamos National Laboratory, MS-E536, Los Alamos, NM 87545, USA

*E-mail: rjin@mailbox.sc.edu

Abstract

Diverse quantum phenomena have been observed in TSn_4 transition metal (T) stannides, including superconductivity, nontrivial topology, and large magnetoresistance at low temperatures. Here, we report the experimental and theoretical investigation of tetragonal β-$IrSn_4$ (space group $I4_1/acd$) with the lattice parameters a = 6.362(3) Å and c = 22.723(0) Å. The temperature dependence of the electrical resistivity indicates that β-$IrSn_4$ is a good metal with Fermi-liquid behavior above the superconducting transition at $T_c \sim 0.7$ K. Magnetic susceptibility measurements indicate it is non-magnetic. However, positive transverse magnetoresistance (MR) with linear field dependence is observed. At $T = 2$ K and $\mu_0 H = 14$ T, the MR reaches 700% without sign of saturation. Shubnikov-de Haas (SdH) oscillations are observed from proximity detector oscillator (PDO) measurements up to 60 T. We experimentally extract several frequencies, and through comparison to first-principles calculations, identify corresponding electronic bands. For H // c, two strong oscillations, $F_1 \approx 109$ and $F_2 \approx 302$ T, allow us to determine effective masses $0.266m_0$ and $0.300m_0$ (m_0 is the free-electron mass), respectively. The topology of these bands is discussed.

Accepted Manuscript

Electronic quantum materials represent a captivating field of exploration in condensed matter physics due to the variety of complex electronic behavior they exhibit and their potential to enable novel electronic devices [1-7]. The additional attraction of nontrivial topological properties, which have a wide range of potential impacts on physics, chemistry, and material science, has selected a subset of correlated-electron systems for more intensive study [1, 5-11]. Recent work from several transition metal stannides with the form TSn_4 (T = Rh, Pd, Pt, etc.) strongly suggests the presence of unusual band structures with nontrivial topology that can trigger an abundance of phenomena, including large magnetoresistance (MR), quantized Hall effect, superconductivity, and strong quantum oscillations [12-20].

Owing to the polymorphic nature of high-tin content compounds, a number of the TSn_4 compounds form polymorphs with different crystal structures [21-26]. For example, $IrSn_4$ forms a trigonal structure (α-$IrSn_4$) with either the $P3_121$ (#152) or $P3_221$ (#154) space group, a tetragonal structure (β-$IrSn_4$), and an orthorhombic structure (γ-$IrSn_4$). According to first-principles calculations, α-$IrSn_4$ represents the ground state, requiring less energy than the other structures [22, 26]. Extremely large MR is observed in α-$IrSn_4$, which shows scaling behavior up to $T = 50$ K that deviates from the standard Kohler's rule [17]. Superconductivity is not observed in resistivity measurements down to $T = 0.1$ K in α-$IrSn_4$, despite its low residual resistivity ($\rho_0 < 0.1$ $\mu\Omega$·cm) [17, 26]. Structurally, β-$IrSn_4$ is more layered, with a lattice constant ratio c/a that is three times higher than those of α-$IrSn_4$ and γ-$IrSn_4$ [20, 22, 26-28]. According to the *ab initio* calculations [29], there is a Van Hove singularity in the electronic structure of β-$IrSn_4$, which is likely responsible for the superconductivity observed in this tetragonal polymorph [18]. This singularity is absent in other forms of $IrSn_4$ [26, 29]. Therefore, a fundamental understanding of

Accepted Manuscript

the electronic properties exhibited by each specific crystal structure of such polymorphic compounds is essential for uncovering rich quantum phenomena.

Among three polymorphs, β-$IrSn_4$ is least investigated. While its band structure is reported in Ref. [29], detailed information such as the quantum oscillation frequency, effective mass, and carrier type for each band is not available. On the other hand, MR for β-$IrSn_4$ is only measured up to 9 Tesla in Ref. [20], which is yet to be confirmed. In this article, we report a combination of experimental and theoretical investigation of the structural, magnetic, and electronic properties of β-$IrSn_4$ single crystals. A large magnetoresistance (MR ~ 700%) is observed at $T = 2$ K and $\mu_0 H = 14$ T. Hall effect measurements reveal a decrease in the carrier concentration (n) at low temperatures. Shubnikov-de Haas (SdH) oscillations are measured at various temperatures, angles, and field via the proximity detector oscillator (PDO) technique up to 60 T. From fast Fourier transformation (FFT) analysis of the SdH oscillations, two bands are identified, which are consistent with first-principles calculations. Information about the Berry phase and effective mass associated with each band is obtained as well.

Our $IrSn_4$ single crystals were grown using the self-flux (Sn) method. Iridium powder (*Alfa Aesar*, 99.9%) and tin granules (*BTC*, 99.9%) were combined in a molar ratio of 1 : 10 in an alumina crucible and sealed in an evacuated (pressure < 50 mTorr) quartz ampoule. The mixture was heated to 1050°C at a rate of 50°C/h, held for 7 days, and cooled to 900°C at a rate of −4 °C/h before being quenched in water. Excess Sn flux was removed by etching with a diluted hydrochloric acid (HCl) solution. The resulting crystals were flat and plate-like with a typical size of 0.8 mm (l) × 0.5 mm (w) × 0.07 mm (t) as shown in Figure 1(a).

The crystal structure was determined through single crystal x-ray diffraction (XRD) using a PANalytical Empyrean x-ray diffractometer (Cu $K\alpha$ radiation, $\lambda_{K\alpha}$ = 1.5418 Å). Electronic

Accepted Manuscript

structure calculations were performed using VASP (Vienna *ab-initio* Simulation Package) based on pseudo-potentials and a plane wave basis set [30]. The exchange-correlation energy functional was described using a PBE (GGA) scheme, taking the spin-orbit interaction (SOI) into account. A self-consistent calculation was performed using a gamma-centered $16 \times 16 \times 4$ k-point mesh with the plane-wave cutoff energy set to 300 eV. The Fermi surface was found using a k-point mesh of $61 \times 61 \times 61$ and visualized with the XCRYSDEN software [31].

Magnetization measurements were carried out in a Magnetic Property Measurement System (MPMS— 7 T, *Quantum Design*). The electrical resistivity, magnetoresistance, and Hall effect were recorded using a Physical Property Measurement System (PPMS— 14 T, *Quantum Design*). The contactless conductivity data was measured at various temperatures and magnetic field applied along different crystal axes using the PDO technique under pulsed magnetic fields of up to 60 T at the National High Magnetic Field Laboratory (NHMFL) [32]. A single crystal of β-$IrSn_4$ was placed on top of an 8-turn pancake coil made of 46-gauge copper wire. The coil is part of an LCR circuit driven by the PDO that has a resonant frequency in the range of 22-30 MHz [33]. Changes in the sample skin depth affect the inductance of the coil, producing a frequency shift Δf. If the sample is a metal, $\Delta f \propto -\Delta\rho$, where $\Delta\rho$ is the corresponding change in the sample resistivity [33]. If the sample is an insulator, Δf is proportional to the magnetic susceptibility change [33]. As the PDO coil's field is localized and near surface, it is extremely sensitive to small changes. Compared resistivity and magnetic susceptibility measurements, PDO provides amplification via probing nonlinear contribution. The coil was mounted on a cryogenic goniometer that permits precise *in-situ* rotation at temperatures down to 0.5 K [34].

According to the single crystal XRD data, depicted in Figure 1(b), our $IrSn_4$ single crystals form in the $MoSn_4$-type tetragonal structure, belonging to the space group $I4_1/acd$. The lattice

Accepted Manuscript

parameters determined are a = 6.362(3) Å and c = 22.723(0) Å, resulting in $c/a \sim 3.57$. These values are consistent with previously reported results for the tetragonal β-$IrSn_4$ phase [18, 20] and differ from the lattice constants for the trigonal and orthorhombic phases [17, 20, 22, 26, 28, 35]. The structure of β-$IrSn_4$ can be described as four stacked layers of $IrSn_8$ antiprisms along the c direction as illustrated in Figure 1(c). This arrangement makes Ir-Sn-Sn-Ir-Sn-Sn-Ir… the favorable path for charge carriers to take in the c direction, suggesting that hybridization between p-p (Sn-Sn) and p-d (Sn-Ir) orbitals significantly affects the electrical transport properties [18, 20].

Figure 2(a) shows the temperature dependence of the zero-field in-plane resistivity (ρ_{xx}) of β-$IrSn_4$ between temperatures T = 2 K and 400 K. At room temperature ($T \approx$ 300 K), $\rho_{xx} \approx$ 0.79 mΩ·cm. This value is roughly one order of magnitude higher than that reported in Ref. [20]. However, we find that the residual resistivity ratio (RRR) is ρ_{xx}(300 K)/ρ_{xx}(2 K) ≈ 263, which is higher than that given in Ref. [20]. The larger RRR strongly suggests that our β-$IrSn_4$ crystals are of high quality and that the exploration of intrinsic low-temperature physical properties may prove fruitful [17-18, 26]. We can quantitatively fit the resistivity data using the Bloch-Grüneisen formula (Eq. (1)) for electron-phonon scattering:

$$\rho_{xx}(T) = \rho_0 + A\left(\frac{T}{\theta_D}\right)^3 \int_0^{\theta_D/T} \frac{x^3}{(e^x-1)(1-e^{-x})^2}\,dx, \qquad (1)$$

where ρ_0 is the residual resistivity, A is a constant describing electron-phonon coupling strength, and θ_D is the Debye temperature. From this fit, represented by the red line in the main panel of Fig. 2(a), we obtain ρ_0 = (0.015 ± 0.001) mΩ·cm, A = (2.1 ± 0.2) mΩ·cm, and θ_D = (201 ± 5) K. Note that Eq. (1) fits our experimental data well over a wide temperature range (60 – 350 K). This fit implies that inter-band scattering is dominant in this system [36]. While the estimated Debye temperature is smaller than the previously reported values, θ_D = 216 K [18] and 256 K [20], we note that the A value is approximately 20 times larger than that obtained in Ref. [18], suggesting

Accepted Manuscript

there is significantly stronger electron-phonon coupling in our sample. In the inset of Fig. 2(a), the low-temperature $\rho_{xx}(T)$ is plotted as $\rho_{xx}(T)$ versus T^2, showing linear behavior persisting up to $T \approx$ 70 K. From fitting (orange line) the low-temperature data using $\rho_{xx} = \rho_0^{LT} + A^{LT}T^2$, we find ρ_0^{LT}= (2.1 ± 0.3) μΩ·cm and A^{LT} = (2.59 ± 0.01) × 10^{-2} μΩ·cm·K^{-2}. A^{LT} is significantly higher than typical values for transition metals (~ 10^{-5} μΩ·cm·K^{-2}), suggesting relatively strong electron-electron interactions in the Fermi liquid state of β-$IrSn_4$ [37]. This behavior may explain the noticeable differences between our low-T data and those in Ref. [18], both in ρ_0^{LT} and the range over which the T^2 behavior persists.

Following the precedents of de Haas-van Alphen (dHvA) oscillations in $PtSn_4$ and superconductivity in $AuSn_4$ and β-$IrSn_4$ [14, 18-20], we examine the magnetic properties of our β-$IrSn_4$ at low field ($\mu_0 H \leq 14$ T). The temperature dependence of the magnetic susceptibility χ, shown in Figure 2(b), is measured between 2 K and 400 K with an applied field of $\mu_0 H = 1$ T along the c-axis in the zero-field-cooling (ZFC) mode. In the entire temperature region, $\chi < 0$, i.e. diamagnetic. To understand the nature of the magnetic response of β-$IrSn_4$, we fit the data using the Curie-Weiss (CW) formula:

$$\chi = \chi_0 + \frac{C}{T-\theta_{CW}}, \quad (2)$$

where χ_0 represents the temperature-independent contribution to the susceptibility, θ_{CW} is the Curie-Weiss temperature, and $C = N_A \mu_{eff}^2 / 3 k_B$ is the Curie-Weiss constant (N_A is the Avogadro constant, k_B is the Boltzmann constant, and μ_{eff} is the effective magnetic moment). We obtain the following parameters from fitting: χ_0 = (−7.770 ± 0.004) × 10^{-3} cm^3/mol, C = (0.0300 ± 0.0002) cm^3·K/mol, and θ_{CW} ~ 0 K. From C, we find the effective magnetic moment μ_{eff} = 0.15μ_B/f.u.. The zero θ_{CW} and small μ_{eff} indicate that there are negligible magnetic interactions in β-$IrSn_4$. By measuring the magnetic field dependence of the magnetization at a fixed temperature, linear

Accepted Manuscript

behavior is observed (not shown), indicating that the diamagnetic behavior results from the core contribution, i.e., a negative χ_0.

Previous investigations of β-$IrSn_4$ reveal a superconducting transition at $T_c \approx 0.9$ K – 1.05 K [18, 20]. From PDO measurements, we observe the resonant frequency (f) increases below a critical field at $T = 0.66$ K. Figure 2(c) shows the change in resonant frequency Δf with applied field at $\theta = 4°$ and 91° from the c-axis at $T = 0.66$ K. Since $\Delta f \propto -\Delta\rho$, the sharp increase in Δf implies that β-$IrSn_4$ enters the superconducting state with an upper critical field of $H_{c2}(4°) \approx 0.17$ T and $H_{c2}(91°) \approx 0.3$ T at $T = 0.66$ K. This value is much higher than that reported in Ref. [18, 20] at the same temperature, suggesting that the zero-field superconducting transition temperature is higher than 1.05 K [20]. The higher H_{c2}, and possibly higher T_c, is likely due to higher sample quality as reflected in the larger RRR.

In Ref. [20], the linear magnetoresistance (MR) was observed for the sample with a slightly lower RRR for H // c at 2 K, which is attributed to open orbits. Figure 3(a) shows the field dependence of the MR up to 14 T at various temperatures. Two distinct features are immediately discernable: (1) at the measured temperatures (2 K $\leq T \leq$ 300 K), the MR varies almost linearly with H without sign of saturation and (2) MR increases with decreasing T reaching ~ 700% at T = 2 K and 14 T. In previous investigations, MR(9 T) ~ 400% at $T = 2$ K was reported for α-$IrSn_4$ (trigonal) [26] and ~ 820% for β-$IrSn_4$ [20]. As discussed in Ref. [20], there linear MR is unlikely due to impurity effect, given that the high RRR for β-$IrSn_4$. In the inset of Fig. 3(a), we plot MR vs. H/ρ_{xx} for each measured temperature with all collapsing into a single curve. This implies that electron scattering is governed by a single relaxation time, even though the MR is not proportional to H^2 according to Kohler's scaling rule [38]. The deviation from the standard H-dependence of the MR may be related to the degree of the electron and hole compensation in semimetallic systems

Accepted Manuscript

[17, 37, 39]. Indeed, in isostructural β-$RhSn_4$ and $PdSn_4$, the linear and unsaturated MR(H) is attributed to their semimetallic nature [12, 15].

To better understand the magnetotransport properties of β-$IrSn_4$, the Hall resistivity ρ_{xy} is measured by applying H // c. Figure 3(b) shows the field dependence of ρ_{xy} between 2 K and 300 K. Similar to that seen in β-$RhSn_4$ [12], ρ_{xy} is positive for β-$IrSn_4$, suggesting the system is hole dominated. While the Hall resistivity varies linearly with $\mu_0 H$ up to 14 T at $T \geq 100$ K, $\rho_{xy}(H)$ deviates from linearity at lower temperatures, which is consistent with observations in Refs. [18, 20]. To estimate the carrier concentration, we extract the Hall coefficient R_H by fitting $\rho_{xy}(H)$ in the linear regime, i.e., $\mu_0 H \leq 1$ T. The value of R_H for each temperature is depicted in Figure 3(c), which exhibits a non-monotonic temperature dependence with a minimum occurring at $T \sim 50$ K. Similar behavior is observed in $PdSn_4$ and $PtSn_4$ and is attributed to contributions from mixed holes and electrons [15, 16]. From R_H, we estimate the carrier concentration as shown Figure 3(d) with $n \sim 2.7 \times 10^{21}$ cm^{-3} at room temperature and $\sim 2.5 \times 10^{21}$ cm^{-3} at 2 K. This minor change in n suggests that the electronic structure is not severely modified by temperature.

From our observations of the behavior in the magnetoresistance and Hall resistivity, we seek further information about the electronic structure to answer our questions: (1) does the Fermi surface consist of both electron and hole bands? and (2) are there open orbits along the c direction as proposed in Ref. [20]? While quantum oscillations are not obvious from low field ($\mu_0 H \leq 14$ T) measurements of χ and MR, they are seen in PDO data measured under higher fields. Figure 4(a) shows the magnetic field dependence of the PDO frequency (f) at $T = 0.66$ K for the angle $\theta(H \wedge c) = 4°$. After the initial sharp drop due to the superconducting transition, f decreases slowly with increasing field at all measured temperatures. We subtract a smooth background (f_{bg}) after fitting the data to a 3rd order polynomial function. Figure 4(b) depicts $\Delta f = f - f_{bg}$ in the high field

Accepted Manuscript

regime where the oscillations are prominent. Here, oscillations with a periodicity proportional to H^{-1} are discerned. Through fast Fourier transform (FFT) analysis, two oscillation frequencies are identified, F_1 = 109 T and F_2 = 302 T (Figure 4(c)). As PDO measures change in the skin depth of the coil, the oscillations in Δf reflect changes in the electrical conductivity, i.e., they are Shubnikov-de Haas (SdH) oscillations [33]. Thus, the two detected frequencies correspond to electron motion in two Fermi surface pockets [40]. We can construct a Landau-level (LL) fan diagram to characterize each pocket further as shown in Figure 4(d), where N is the LL index. According to the Lifshitz-Onsager quantization criterion, $N = \gamma + \frac{F_{fit}}{H}$, with $\gamma = \phi_B/2\pi + \delta$. Here, ϕ_B is the Berry phase and $\delta = 0, \frac{+1}{8}, \frac{-1}{8}$, depending on carrier type and dimensionality of the Fermi surface [41]. By fitting the $N(H^{-1})$ data using the Lifshitz-Onsager formula, we obtain γ and F_{fit} for each oscillation, which are listed in Table I. As displayed in Fig. 4(c), the FFT amplitude for each oscillation decreases with increasing temperature. While the FFT spectrum is dominated by the lower frequency (F_1), the higher frequency (F_2) can also be well resolved up to T = 45 K. Figures 4(e) and 4(f) display the temperature dependence of the FFT amplitude for F_1 and F_2, respectively. From a fit of the temperature dependence of the FFT amplitude to the thermal damping factor $R_T = \frac{A'\left(\frac{m^*}{m_0}\right)T}{sinh\left(A'\left(\frac{m^*}{m_0}\right)T\right)}$ (A' is a T-independent constant) of the Lifshitz-Kosevich formula [40], we obtain the effective masses m^*_{F1}= 0.266m_0 and m^*_{F2} = 0.300m_0, where m_0 is the free-electron mass.

To understand the nature of the SdH oscillations, we perform electronic structure calculations. Using lattice relaxation calculations, we find that the system crystallizes in a tetragonal structure containing 40 atoms in the unit cell as shown in Figure 1(a). However, we obtain that $a = b$ = 6.424 Å and c = 23.108 Å, slightly larger than those obtained from prior DFT

Accepted Manuscript

calculations [29] and our experimental work. The band structure is calculated along the high-symmetry directions of the tetragonal lattice using the path $\Gamma - X - M - \Gamma - Z - R - A - Z|Z - R|M - A$, as shown in Figure 5. All bands not crossing the Fermi level are displayed in gray. There are eight bands (Bands I – VIII) contributing to the Fermi surface. Similar to prior work [29], there are several Dirac cones in the vicinity of the Fermi energy, which are denoted by circles in Figure 5. The gaps in the encircled Dirac cones are ~ 10 – 20 meV, also in agreement with Ref. [29]. The cones close to the Fermi energy distinguish β-$IrSn_4$ from many other topological semimetals with potential for future applications. The Fermi surface topology is presented in Figure 6 with both top (b_1, b_2) and side (b_1, b_3) views. Similar to a previously constructed Fermi surface [29], the bands exhibit mostly two-dimensional characteristic with open orbits along the *c*-direction. For each band, the expected oscillation frequency, effective mass, and carrier type are listed in Table I for H // c.

To figure out the origin of the experimentally observed oscillations at various angles, we plot the angle dependence of the frequencies obtained from FFT analysis, LL fan diagram fitting, and the theoretical frequency calculations in Figure 7. Through comparison, we find that Band II (Fig. 7(a)), IV (Fig. 7(b)), and VII (Fig. 7(d)) can have the oscillation F_1, and Band VII and VIII (Fig. 7(d)) can have F_2 for H // c. However, the angular dependence of the estimated frequency does not seem to close to that of F_{th} for Band II, which is thus not included in Table I. On the other hand, while not obvious in Fig. 4(c), the calculated frequencies for Band III match well with experimental data as shown in Fig. 7(b). $F_{th}(H // c) = 261$ T could be hidden under the broad peak marked as F_2 in Fig. 4(c). Interestingly, all experimentally identified possible bands have electron character, as can be seen from Table I. Considering β-$IrSn_4$ is a hole-dominated system (Fig. 3 and Refs. [18, 20]), SdH oscillations from hole bands are likely too weak to be experimentally probed.

Accepted Manuscript

As listed in Table I, all calculated hole bands have high frequencies except Band V (which consists of a small pocket). In view of the FFT shown in Fig. 4(c), the strongest peak centered at F_1 is broad. Low-frequency (< 200 T) oscillations with much smaller amplitudes than the F_1 oscillation are difficult to be identified from FFT. On the other hand, the experimentally identified $F_{ex}(H // c)$ ~ 700 T may result from a hole band (e.g. VI) but is too weak to be traced as the crystal orientation is rotated. Nevertheless, given the system involves multiple bands with both electron and hole pockets, the Hall coefficient should be expressed as $R_H = \frac{1}{e}\frac{n_h\mu_h^2 - n_e\mu_e^2}{(\mu_h n_h + \mu_e n_e)^2}$, where n_h is the hole carrier concentration, n_e denotes the electron concentration, μ_h is the hole mobility, and μ_e is the electron mobility. Even if n_h is lower than n_e, if μ_h is much higher than μ_e, the sign of R_H is determined by $n_h\mu_h^2 - n_e\mu_e^2$, leading to a positive sign. The nonlinear H dependence of ρ_{xy} below 50 K (Fig. 3(b)) reflects the change of $n_h\mu_h^2 - n_e\mu_e^2$. Despite experiment limitation, both calculated and experimental data presented in Fig. 7 will guide future work for β-$IrSn_4$.

The γ values for some of the frequencies identified through LL fan diagrams are included in Table I. Based on theoretical calculations, we can further assign the δ value for each case. The Berry phase ϕ_B ($H // c$) can thus be estimated as listed in Table I. It seems that Bands III, VI, and VII have a $\phi_B(H // c)$ close to π. In view of the band structure in Fig. 5, Band III is indeed associated with the three Dirac cones highlighted by three circles. If it dominates the electrical transport, the observed linear MR (Fig. 3(a)) can then be explained. While the large and linear MR could be related to open orbits [20, 42], we notice that (1) the linear MR is only seen for $H // c$ in β-$IrSn_4$ [20] and (2) the MR is the smallest for $H \perp c$ [20] at which point the open orbits become most impactful (see Fig. 6). Therefore, the linear MR shown in Fig. 3(a) is unlikely due to open orbits. According to Ref. [43], the ratio MR/H scales linearly with the Berry curvature near the Fermi

Accepted Manuscript

level. This is indeed the case for β-$IrSn_4$ (see Fig. 5). Further, the decrease of MR with increasing T is due to increased scattering or slowing down of carriers [43].

In summary, we have successfully grown $IrSn_4$ single crystals with the tetragonal structure, i.e., β-$IrSn_4$. Through both electrical resistivity and PDO measurements, we find that β-$IrSn_4$ is a metal with a superconducting ground state. While it is non-magnetic and clean, as reflected by a high RRR, a large transverse magnetoresistance of ~ 700% is observed at $T = 2$ K and $\mu_0 H = 14$ T. Although the MR at different temperatures and fields collapses into a single curve, its field dependence is nearly linear, not conforming to the standard Kohler's expression. By analyzing data collected from PDO measurements up to 60 T, Shubnikov-de Haas oscillations with various frequencies at different applied field directions are observed. Based on first-principles calculations, the Fermi surface of β-$IrSn_4$ consists of eight bands with band crossings along $\Gamma - X - M - \Gamma$. The experimentally observed frequencies $F_1 = 109$ T and $F_2 = 302$ T are most likely from Bands IV (F_1), VI (F_1), VII (F_1), VII (F_2), and VIII (F_2), which all have electron character. By constructing Landau level fan diagrams, Berry phase for some bands can be extracted, pointing Bands III, VI, and VII with possible nontrivial topology. The nontrivial topology helps understand the linear MR (H // *c*) observed in a wide temperature range, similar to that reported in Ref. [43]. Further work is necessary to improve the experimental resolution for distinguishing oscillations and the accuracy of DFT calculations. According to Ref. [44], the van der Waals force can be important when calculating the band structures of layered materials, which may be relevant to β-$IrSn_4$.

Acknowledgements

This work was partially (RJ) supported by the grant No. DE-SC0024501 funded by the U.S. Department of Energy, Office of Science. J.S. acknowledges support from the DOE BES program "Science at 100T," which permitted the design and construction of specialized

Accepted Manuscript

equipment used in the high field studies. A portion of this work was performed at the National High Magnetic Field Laboratory (NHMFL), which is supported by National Science Foundation Cooperative Agreements No. DMR-1644779 and DMR-2128556 and the Department of Energy (DOE).

Accepted Manuscript

References:

[1] S. R. Lee, P. A. Sharma, A. L. Lima-Sharma, W. Pan, and T. M. Nenoff, Topological quantum materials for realizing Majorana quasiparticles, Chem. Mater. **31**, 26 (2019).

[2] C. Day, Devices based on the fractional quantum Hall effect may fulfill the promise of quantum computing, Physics Today **58**, 10 (2005).

[3] W. Zhu, D. N. Sheng, and F. D. M. Haldane, Minimal entangled states and modular matrix for fractional quantum Hall effect in topological flat bands, Phys. Rev. B **88**, 035122 (2013).

[4] K.-L. Chiu, D. Qian, J. Qiu, W. Liu, D. Tan, V. Mosallanejad, S. Liu, Z. Zhang, Y. Zhao, and D. Yu, Flux tunable superconducting quantum circuit based on Weyl semimetal $MoTe_2$, Nano Lett. **20**, 8469 (2020).

[5] W.-C. Chien, S.-J. Jhan, K.-L. Chiu, Y.-X. Liu, E. Kao, and C.-R. Chang, Cryogenic materials and circuit integration for quantum computers, Journal of Electronic Materials **49**, 6845 (2020).

[6] A. Zitolo et al., Identification of catalytic sites in cobalt-nitrogen-carbon materials for the oxygen reduction reaction, Nat. Commun. **8**, 957 (2017).

[7] A. K. Zvedin and V. A. Kotov, *Modern magneto-optics and magneto-optical materials* (Taylor & Francis: New York, 1997).

[8] J. E. Kunzler, E. Buehler, F. S. L. Hsu, and J. H. Wernick, Superconductivity in Nb_3Sn at high current density in a magnetic field of 88 kgauss, Phys. Rev. Lett. **6**, 89 (1961).

[9] S. A. Wolf, A. Y. Chtchelkanova, and D. M. Treger, Spintronics- a retrospective and perspective, IBM J. Res. & Dev. **50**, 102 (2006).

[10] A. A. Burkov, M. D. Hook, and L. Balents, Topological nodal semimetals, Phys. Rev. B **84** 235126 (2011).

Accepted Manuscript

[11] R. Pöttgen, Stannides and intermetallic tin compounds - fundamentals and applications, Z. Naturforsch. **61b**, 677 (2006).

[12] X. Z. Xing, C. Q. Xu, N. Zhou, B. Li, J. Zhang, Z. X. Shi, and X. Xu, Large linear magnetoresistance in transition-metal stannide β-$RhSn_4$. Appl. Phys. Lett. **109**, 122403 (2016).

[13] X. Luo et al., Origin of the extremely large magnetoresistance in topological semimetal $PtSn_4$, Phys. Rev. B **97**, 205132 (2018).

[14] E. Mu, H. Ko, G. J. Miller, G. D. Samolyuk, S. L. Bud'ko, P. C. Canfield, Magnetic field effects on transport properties of $PtSn_4$, Phys. Rev. B **86**, 079909 (2012).

[15] C. Q. Xu et al., Enhanced electron correlations in the binary stannide $PdSn_4$: a homologue of the Dirac nodal arc semimetal $PtSn_4$, Phys. Rev. Mat. **1**, 064201 (2017).

[16] N. H. Jo et al., Extremely large magnetoresistance and Kohler's rule in $PdSn_4$: a complete study of thermodynamic, transport, and band-structure properties. Phys. Rev. B **96**, 165145 (2017).

[17] R. Omura, E. Suto, N. Nakamura, R. Higashinaka, T. D.Matsuda, and Y. Aoki, Single crystal growth and anomalous magnetoresistance of chiral crystal α−$IrSn_4$, Proceedings of the International Conference on Strongly Correlated Electron Systems (SCES2019), 2020.

[18] V. H. Tran, Z. Bukowski, P. Wísniewski, L. M. Tran, and A. J. Zaleski, Observation of superconductivity in the intermetallic compound β-$IrSn_4$, Journal of Physics: Condensed Matter **25**, 155701 (2013).

[19] D. Shen, C. N. Kuo, T. W. Yang, N. Chen, C. S. Lue, and L. M. Wang, Two-dimensional superconductivity and magnetotransport from topological surface states in $AuSn_4$ semimetal, Communications Materials **1**, 56 (2020).

Accepted Manuscript

[20] N. Ahmad, S. Shimada, T. Hasegawa, H. Suzuki, M. A. Afzal, N. Nakamura, R. Higashinaka, T. D. Matsuda, Y. Aoki, Linear magnetoresistance and type-I superconductivity in β-$IrSn_4$, J. Phys. Soc. Jpn. **93**, 044706 (2024).

[21] J. Nylén, F.J. García, B.D. Mosel, R. Pöttgen, and U. Häussermann. Structural relationships, phase stability and bonding of compounds $PdSn_n$ (n=2, 3, 4), Solid State Sciences **6**, 147, (2004).

[22] E. Nordmark, O. Wallner, and U. Häussermann, Polymorphism of $IrSn_4$, Journal of Solid-State Chemistry **168**, 34 (2002).

[23] A. V. Oleinich and B. G. Strongin, High-temperature polymorphism of tin, Soviet Physics Journal **32**, 162 (1989).

[24] A. Lang and W. Jeitschko, Transition-metal stannides with high tin content: Os_4Sn_{17}, $RhSn_3$, $RhSn_4$, and $IrSn_4$, J. Mater. Chem. **6**, 1897 (1996).

[25] T. Fickenscher, S. Lösel, H. Hillebrecht, J. Kösters, T. Block, G. Heymann, H. Huppertz, and R. Pöttgen, $RhSn_3$ and the modifications of $RhSn_4$ – structure and ^{119}Sn Mössbauer spectroscopic characterization, Z. Naturforsch. **74**, 203 (2019).

[26] N. Nakamura, A. Yanuma, Y. Chiba, R. Omura, R. Higashinaka, H. Harima, Y. Aoki, T. D. Matsuda, Fermi surface and superconducting properties of α-$IrSn_4$, α-$RhSn_4$, $IrGe_4$, $RhGe_4$ with trigonal chiral structure, J. Phys. Soc. Jpn. **92**, 034701 (2023).

[27] A.B. Pippard, *Magnetoresistance in Metals*, Cambridge University Press, Cambridge (1989).

[28] V. Larchev, S. Popova, The new phases $IrSn_4$ and $RhGe_4$ formed by high pressure treatment, J. Less-Common Met. **98**, L1 (1984).

Accepted Manuscript

[29] T. L. Mai, V. H. Tran, *Ab initio* investigation of electronic structure and optical properties of $IrSn_4$, RSC Adv. **12**, 17882 (2022).

[30] G. Kresse and J. Furthmüller, Efficiency of ab-initio total energy calculations for metals and semiconductors using a plane-wave basis set, Computational Materials Science **6**, 15 (1996).

[31] A. Kokalj, XCrySDen – a new program for displaying crystalline structures and electron densities, J. Mol. Graphics Modell. **17**, 176 (1999).

[32] J. Singleton, C. H. Mielke, A. Migliori, G. S. Boebinger, and A. H. Lacerda, The national high magnetic field laboratory pulsed-field facility at Los Alamos national laboratory, Physica B: Condensed Matter **346**, 614 (2004).

[33] S. Ghannadzadeh, M. Coak, I. Franke, P. A. Goddard, J. Singleton, J. L. Manson, Measurement of magnetic susceptibility in pulsed magnetic fields using a proximity detector oscillator Rev. Sci. Instrum **82,** 113902 (2011).

[34] X. Willis, X. Ding, J. Singleton and F. F. Balakirev, Cryogenic goniometer for measurements in pulsed magnetic fields fabricated via additive manufacturing technique, Rev. Sci. Instrum. **91**, 036102 (2020).

[35] B. Kunnen, D. Niepmann, W. Jeitschko, Structure refinements and some properties of the transition metal stannides Os_3Sn_7, Ir_5Sn_7, $Ni_{0.402(4)}Pd_{0.598}Sn_4$, α-$PdSn_2$ and $PtSn_4$, J. Alloys Comp. **309**, 1 (2000).

[36] A. H. Wilson, R. H. Fowler, The electrical conductivity of the transition metals, Proceedings of the Royal Society A **167**, 580 (1938).

[37] K. Miyake, T. Matsuura, and C. M. Varma, Relation between resistivity and effective mass in heavy-fermion and A15 compounds, Solid State Comm. **71**, 12 (1989).

Accepted Manuscript

[38] M. Kohler, Ann. Physik **32**, 211 (1938).

[39] J. Xu, F. Han, T. T. Wang, L. R. Thoutam, S. E. Pate, M. Li, X. Zhang, Y. L. Wang, R. Fotovat, U. Welp, X. Zhou, W. K. Kwok, D. Y. Chung, M. G. Kanatzidis, Z. L. Xiao, Extended Kohler's Rule of Magnetoresistance, Phys. Rev. X **11**, 041029 (2021).

[40] David Shoenberg, *Magnetic Oscillations in Metals* (Cambridge University Press, Cambridge 1984).

[41] C. Li et al., Rules for phase shift of quantum oscillations in topological nodal-line semimetals, Phys. Rev. Lett. **120**, 146602 (2018).

[42] B. Wu, V. Barrena, H. Suderow, I. Guillamon, Huge linear magnetoresistance due to open orbits in γ-$PtBi_2$, Phys. Rev. Res. **2**, 022042 (2020).

[43] S. Zhang, Y. Wang, Q. Zeng et al., Scaling of Berry-curvature monopole dominated large linear positive magnetoresistance, PNAS **119**, E2208505119 (2022).

[44] A. Rajbanish, J. Xing, D. Gong, W. A. Shelton, R. Jin, An alternative ground state of $MnBi_2Te_4$ obtained by magnetic annealing, APL Mater. **13**, 101110 (2025).

Accepted Manuscript

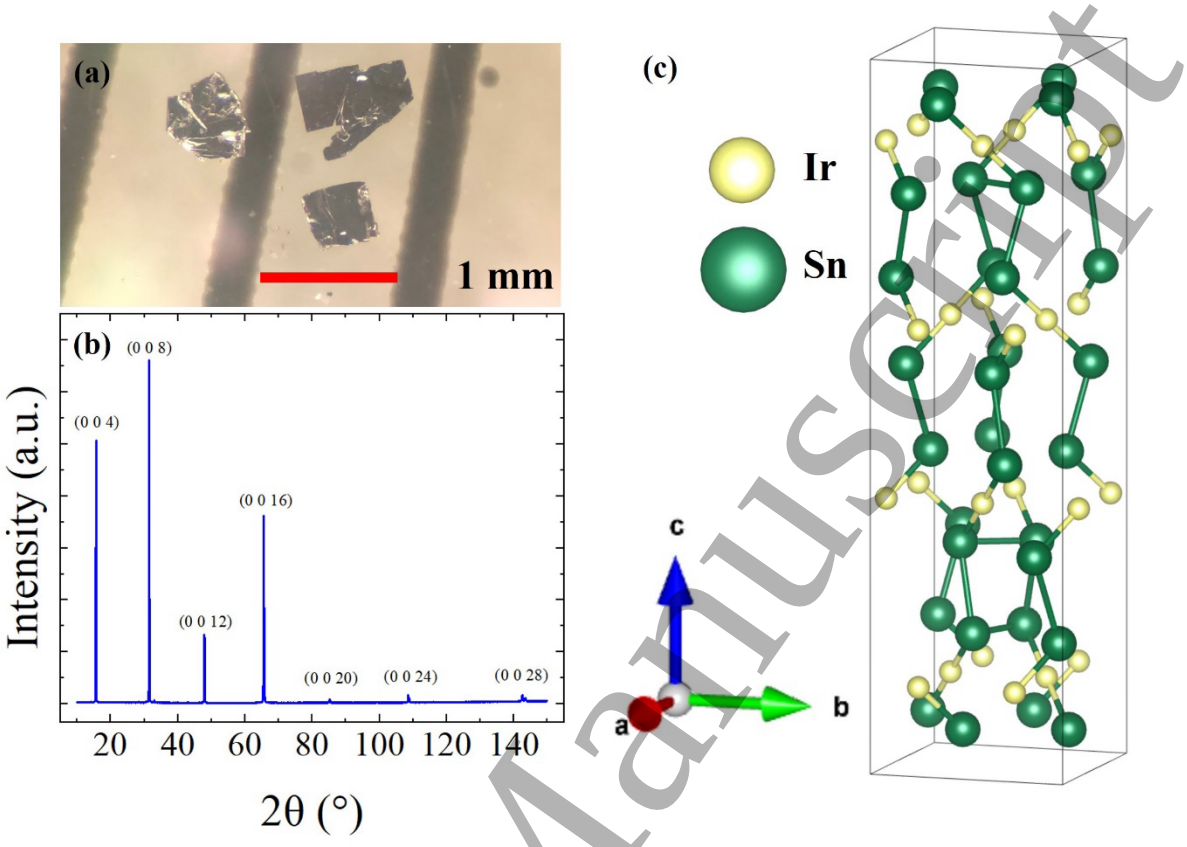

Figure 1. (a) β-$IrSn_4$ single crystals. (b) Room-temperature x-ray diffraction pattern on the surface of a single crystal. (c) Crystal structure of β-$IrSn_4$.

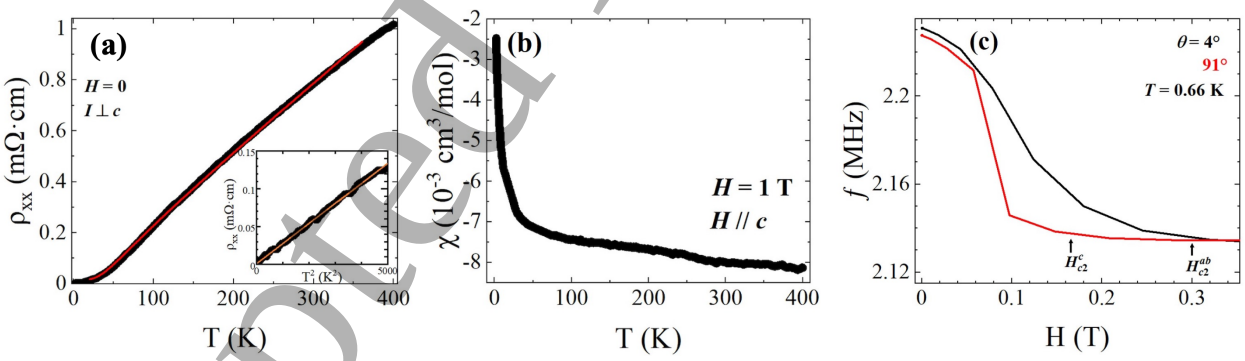

Figure 2. (a) Temperature dependence of the in-plane electrical resistivity (ρ_{xx}). The red line in the main panel represents a fit to the Bloch-Grüneisen formula described in the text. Inset: ρ_{xx} versus T^2 at low temperatures and the orange line represents a linear fit between 1.9 and 70 K as described in the text. (b) Temperature dependence of the magnetic susceptibility of β-$IrSn_4$ measured under an applied field of $H = 1$ T in field-cooling (FC) mode with an orientation where H // c. (c) Magnetic field dependence of the resonant frequency (f) at $T = 0.66$ K and indicated angles.

Accepted Manuscript

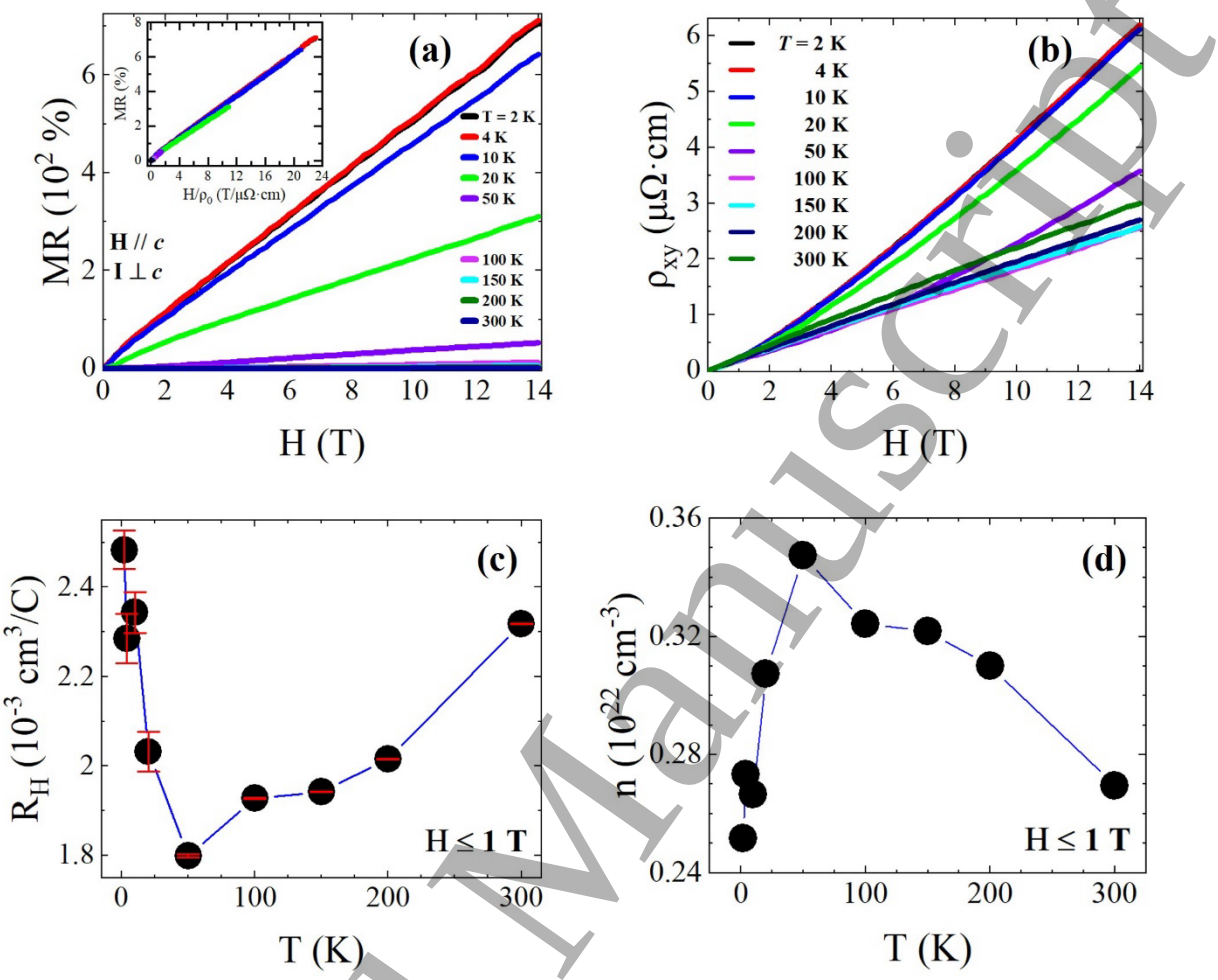

Figure 3. (a) Transverse MR vs. H at indicated temperatures. Inset: Kohler plot for β-$IrSn_4$ with the MR at all temperatures following into the same line. (b) Magnetic field dependence of the Hall resistivity (ρ_{xy}) at indicated temperatures for H // c. (c) Temperature dependence of the Hall coefficient (R_H) obtained below 1 T. (d) Temperature dependence of the carrier concentration n described in the text.

Accepted Manuscript

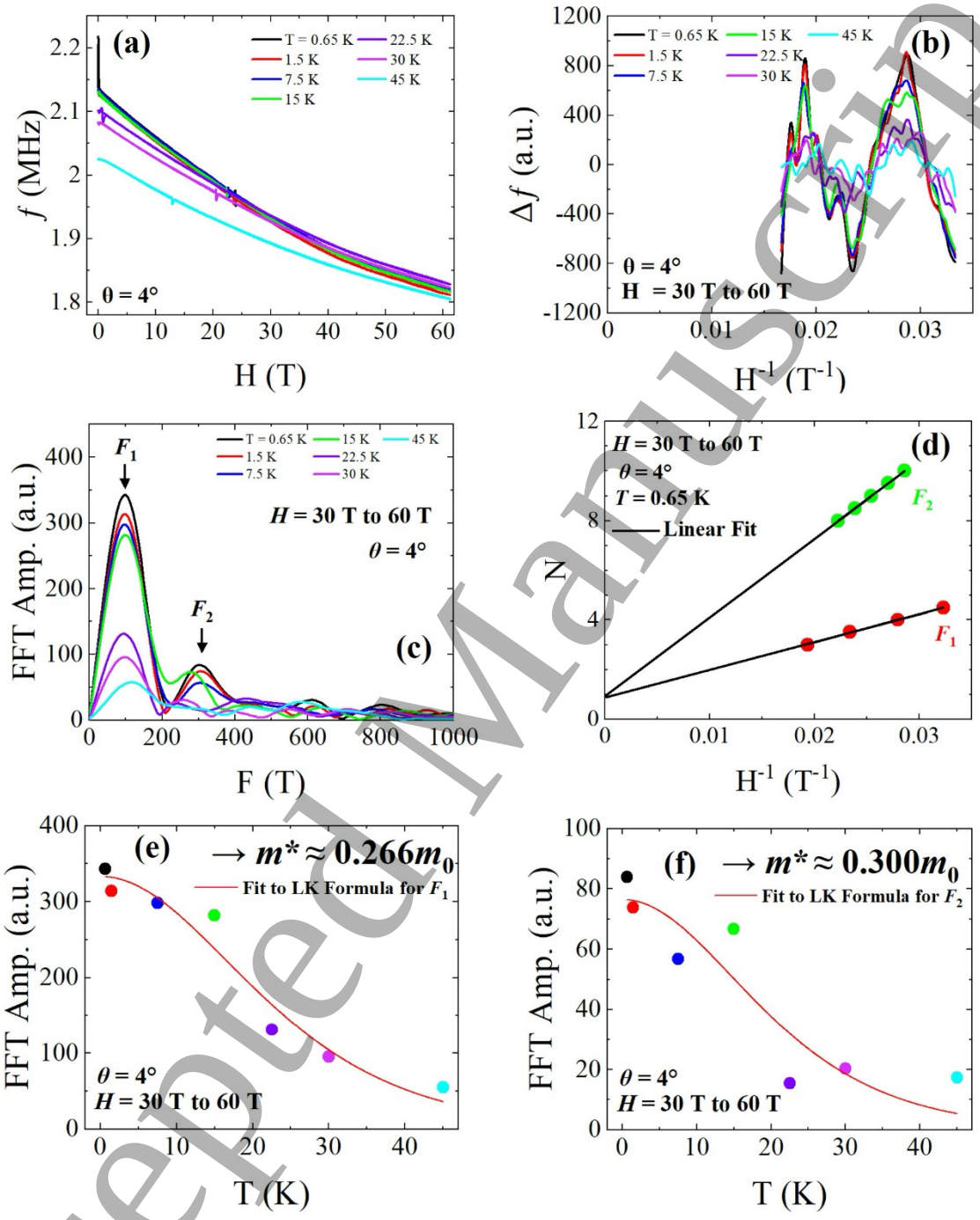

Figure 4: (a) Magnetic field dependence of f with H nearly parallel to the c-axis (θ = 4°). (b) Shubnikov-de Haas (SdH) oscillations at various temperatures obtained through background subtraction. (c) FFT of data shown in (b). (d) Landau level (LL) fan diagram for two oscillations at T = 0.65 K. (e) Temperature dependence of the FFT amplitude for F_1 ~ 109 T at θ = 4°. (f) Temperature dependence of the FFT amplitude for F_2 ~ 302 T at θ = 4°.

Accepted Manuscript

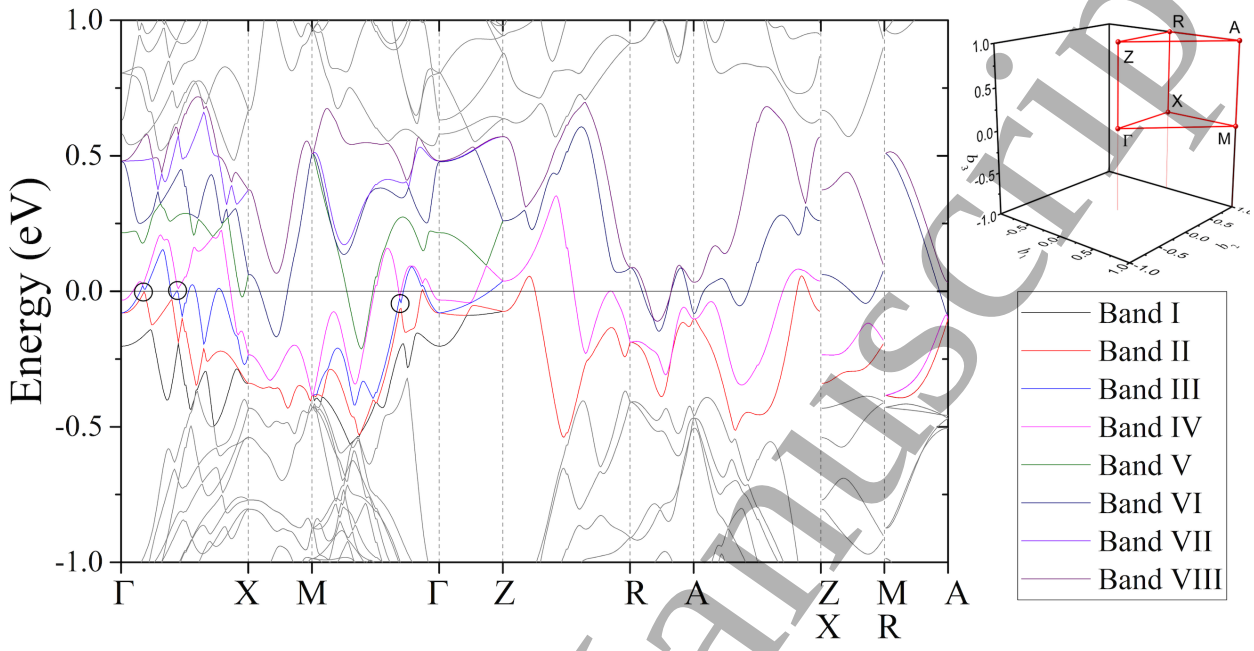

Figure 5: Band structure of β-$IrSn_4$ calculated accounting for spin-orbit interaction. Circles indicate the locations of Dirac cones. Special points of the Brillouin zone are defined. Bands not crossing the Fermi energy are shown in gray.

Accepted Manuscript

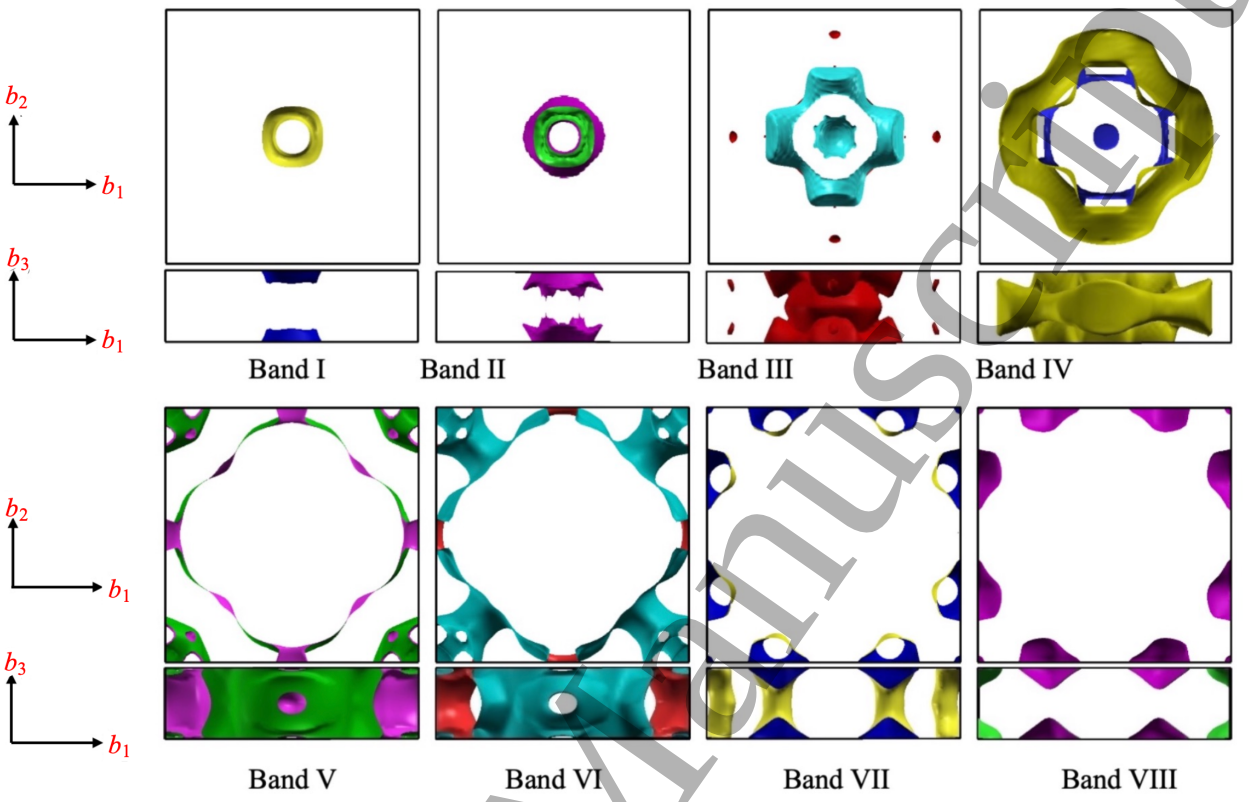

Figure 6: Topology of the Fermi surface of β-$IrSn_4$ consisting of eight bands with both top (b_1, b_2) and side views (b_1, b_3).

Accepted Manuscript

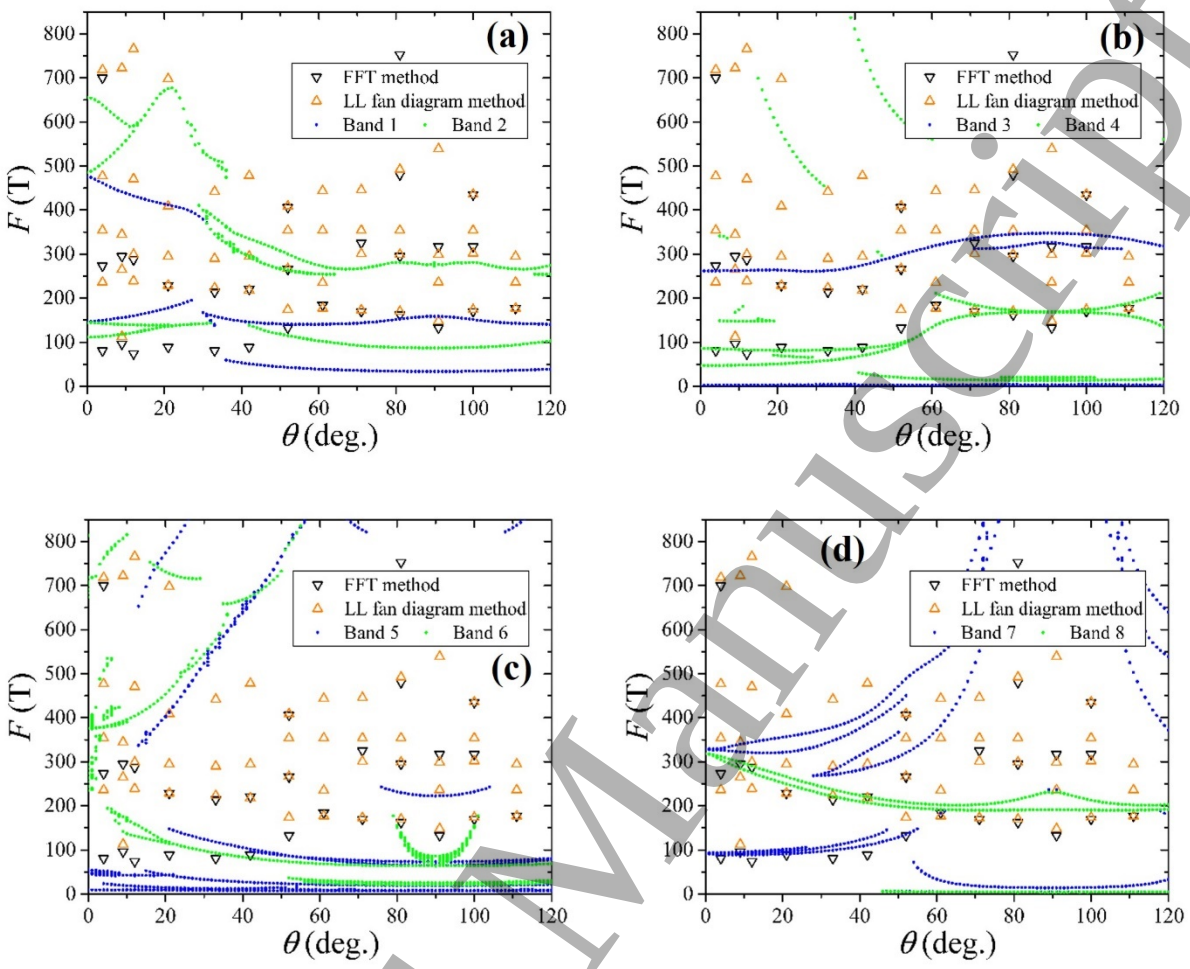

Figure 7: Angular dependence of measured and calculated SdH frequencies. Calculated frequencies originating from different bands are shown in different plots for clarity: (a) Bands I and II; (b) Bands III and IV; (c) Bands V and VI; and (d) Bands VII and VIII.

Accepted Manuscript

Table I: Parameters obtained from the SdH oscillations for H // c including the oscillation frequency (F), intercept (γ), effective mass (m^*), and corresponding Berry phase (ϕ_B). The calculated SdH frequency (F), effective mass (m^*) and carrier type (electron(e)/hole(h)) character are also listed.

Band	Experiment (H // c)					Theory (H // c)		
	F_{FFT}(T)	γ	δ	ϕ_B (π)	m^*/m_0	F_{th}(T)	m^*/m_0	e/h
I						147	0.2781	e
						476	0.2637	h
II						111	0.2830	e
						144	0.2787	e
						504	0.2676	h
						679	0.5312	h
III	~250	0.62	-1/8	1.49		261	0.7849	e
						1221	0.3321	h
						1934	0.7337	h
IV						47	0.2197	e
	109	0.79	-1/8	1.83	0.266	86	0.2590	e
						1494	0.4237	h
						1853	0.3952	e
						1952	0.7293	h
V						49-56	0.3269-0.4176	h
						938	0.4039	h
VI						235	1.3746	e
						244	1.4101	e
						255	1.5467	e
						264	1.6454	e
						274	1.7855	e
						284	2.1411	e
	302	0.96	1/8	1.67		293	3.1404	e
						376	0.3125	e
						674	2.7291	h
						683	2.3082	h
						692	1.8769	h
	~700	0.66	1/8	1.07		701	1.752	h
						708	1.5659	h
						718	1.4456	h
						814	0.8133	h
						814	0.8051	h
VII						91	0.1510	e
	109	0.79	1/8	1.33	0.266	94	0.1383	e
	302	0.96	1/8	1.67	0.300	328	0.2813	e
						330	0.2854	e
VIII	302	0.96	−1/8	0.23	0.300	318	0.2745	e

Accepted Manuscript